J Adv Ceram

Research Article

Hydrothermal synthesis of $MoSe_2/Ni_3Se_4$ heterostructures anchored on high-entropy $M_4C_3T_x$ (M = Ti, V, Mo, Nb, Ta) with superior hydrogen evolution reaction activity

Haoran Zou[1,2], Wen Zhang[1,2,✉], Fangze Chen[1,2], Chao Zhang[1], Jinyong Zhang[2], Lin Ren[2], Weimin Wang[2], Fan Zhang[1,2,✉], Zhengyi Fu[1,2]

Cite this article: Zou H, Zhang W, Chen F, et al. *J Adv Ceram* 2026, **15**(2): 9221235. https://doi.org/10.26599/JAC.2025.9221235

ABSTRACT: Developing hydrogen evolution reaction (HER) electrocatalysts with high activity in both acidic and alkaline media is of great significance for adapting to diverse electrolytic environments. In this study, $MoSe_2$ and Ni_3Se_4 nanosheets were successfully composited on high-entropy $M_4C_3T_x$ MXene (M = Ti, V, Mo, Nb, Ta) via a hydrothermal method, constructing a novel heterostructured catalyst. This design leverages the excellent conductivity and multielement synergistic effect of high-entropy MXenes, which not only facilitates electron transport but also provides a robust platform for the uniform distribution of $MoSe_2$ and Ni_3Se_4 nanosheets, thereby exposing abundant active sites. Electrochemical tests indicate that the catalyst exhibits excellent HER performance in both 0.5 M H_2SO_4 and 1.0 M KOH electrolytes. Specifically, under acidic conditions, $MoSe_2/Ni_3Se_4/M_4C_3T_x$ shows an overpotential of only 67 mV at a current density of 10 mA·cm^{-2} with a Tafel slope of 68.7 mV·dec^{-1}, while under alkaline conditions, the overpotential at 10 mA·cm^{-2} is 73 mV with a Tafel slope of 77.8 mV·dec^{-1}. Moreover, the catalyst demonstrates excellent long-term stability in both acidic and alkaline media. This work provides a new strategy for designing efficient and stable HER catalysts suitable for harsh acid–base environments.

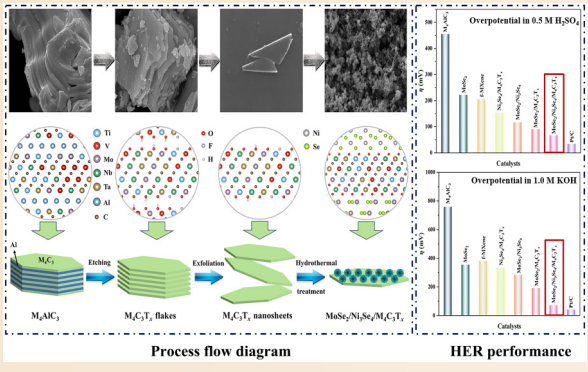

KEYWORDS: high-entropy MXene; hydrogen evolution reaction (HER); heterostructure electrocatalyst; $MoSe_2/Ni_3Se_4/M_4C_3T_x$

1 Introduction

With the intensification of the global energy crisis and environmental pollution, the development of sustainable and clean energy technologies has become a focal point of current research [1,2]. Among them, hydrogen energy is considered one of the most promising clean energy sources due to its renewability, high energy density, and zero carbon emissions [3,4]. To date, large-scale hydrogen production still relies primarily on fossil fuels, which results in significant greenhouse gas emissions. In contrast, the electrochemical hydrogen evolution reaction (HER) via water splitting offers an efficient and environmentally friendly route for hydrogen generation [5–7]. However, the HER process suffers from sluggish kinetics and thus requires efficient electrocatalysts to reduce the overpotential and accelerate the reaction rate. At present, noble metals such as Pt are recognized as the most effective HER electrocatalysts, but their high cost and scarcity hinder widespread application [8–10]. Therefore, the development of efficient, stable, and cost-effective nonnoble metal catalysts has emerged as a key research priority in this field.

Currently, transition metal chalcogenides (TMCs) have attracted widespread attention due to their excellent electrochemical properties and abundant reserves in the Earth's crust. Among them, $MoSe_2$ is regarded as a highly promising electrocatalyst owing to its unique layered structure, tunable physicochemical properties, and nearly thermoneutral hydrogen adsorption Gibbs free energy ($\Delta G_H \approx 0.05$ eV) [11–13]. It is well established that the essence of the HER lies in the effective adsorption and conversion of reactants at active sites—only these sites are truly involved in the catalytic process. For $MoSe_2$, the catalytic activity is primarily localized at the edge sites, while the basal planes are largely catalytically inert. Moreover, excellent electronic conductivity is another critical factor for efficient HER electrocatalysts. However, as a semiconductor, $MoSe_2$ exhibits much lower electrical conductivity than noble metals, which leads to sluggish charge transfer kinetics and consequently limits its

[1] Hubei Longzhong Laboratory, Wuhan University of Technology Xiangyang Demonstration Zone, Xiangyang 441000, China. [2] State Key Laboratory of Advanced Technology for Materials Synthesis and Processing, Wuhan University of Technology, Wuhan 430070, China.

✉ Corresponding authors. E-mail: W. Zhang, wenzhang0407@126.com; F. Zhang, zhfan@whut.edu.cn

Received: October 22, 2025; Revised: December 18, 2025; Accepted: December 22, 2025

overall catalytic performance. The HER process typically involves three fundamental steps: hydrogen adsorption, electron transfer (reduction), and hydrogen molecule desorption [14]. Catalysts composed of a single component often exhibit high efficiency in one of these steps but may be limited in others. In contrast, heterogeneous hybrid materials, by incorporating multiple chemical components and interfacial interactions, hold great promise for achieving synergistic optimization across all reaction steps, thereby overcoming the intrinsic limitations of single-phase catalysts. In recent years, Ni-based catalysts have been explored by researchers for combination with $MoSe_2$ in various forms to achieve enhanced HER performance due to their excellent electron transport capabilities [15–17]. For example, Zhou *et al.* [18] anchored ternary molybdenum sulfoselenide ($MoS_{2(1-x)}Se_{2x}$) onto a highly conductive porous $NiSe_2$ framework, resulting in significantly enhanced HER catalytic performance. Wu *et al.* [19] successfully prepared $MoSe_2$–Ni_3Se_4 hybrid nanoelectrocatalysts via a seed-mediated solution method. This hybrid catalyst exhibited outstanding HER performance under acidic conditions at a Mo:Ni molar ratio of 2 : 1, with an onset overpotential of only 140 mV, an overpotential of 201 mV at a current density of 10 mA·cm^{-2}, and a low Tafel slope of 57 mV·dec^{-1} [19]. The study by Guo *et al.* [20] revealed a continuous charge distribution near the Fermi level in both $NiSe_2$ and Ni_3Se_4, with Ni_3Se_4 exhibiting a relatively higher distribution at the Fermi level, indicating that Ni_3Se_4 may possess higher HER activity.

Another effective strategy to enhance catalytic performance is the incorporation of highly conductive support materials. MXenes, a family of two-dimensional transition metal carbides, nitrides, and carbonitrides with the general formula $M_{n+1}X_nT_x$ (n = 1–3; M stands for Ti, Cr, or Nb; X is C and/or N; T_x is the surface functional group (such as –F or –OH)), have attracted considerable attention owing to their excellent electrical conductivity and abundant surface functional groups [21–24]. Currently, most MXenes contain only one or two transition metals. However, numerous studies on high-entropy materials have shown that doping with multiple transition metals can yield diversified structures, tunable compositions, and significant performance enhancements. Introducing the high-entropy design concept into MXenes induces lattice distortions, which in turn generate more active sites and improve electrical conductivity [25–29]. For example, Du *et al.* [26] selectively etched $(Ti_{1/5}V_{1/5}Zr_{1/5}Nb_{1/5}Ta_{1/5})_2AlC$ to obtain $(Ti_{1/5}V_{1/5}Zr_{1/5}Nb_{1/5}Ta_{1/5})_2CT_x$. Due to the substantial mechanical strain within the atomic layers, this material effectively guides uniform lithium nucleation and dendrite-free growth, achieving remarkable stability over 1200 hours of cycling and excellent deep stripping-plating performance at a current density of 20 mAh·cm^{-2} in lithium-ion batteries [26].

In this study, two-dimensional nanoscale high-entropy $M_4C_3T_x$ MXene (M = Ti, V, Mo, Nb, Ta) was synthesized by selectively etching the self-synthesized high-entropy M_4AlC_3 phase and used as a substrate. Subsequently, $MoSe_2$/Ni_3Se_4 composites were successfully grown on the $M_4C_3T_x$ surface via a simple hydrothermal method, forming $MoSe_2$/Ni_3Se_4/$M_4C_3T_x$ heterostructures to enhance HER activity. The composition and microstructure of the materials were characterized using X-ray diffraction (XRD), scanning electron microscopy (SEM), transmission electron microscopy (TEM), and X-ray photoelectron spectroscopy (XPS). The HER activity in both acidic and alkaline media was evaluated using electrochemical measurements, and the mechanisms underlying the enhanced activity were also investigated.

2 Experimental

2.1 Chemical reagents

All chemical reagents used in this study were of analytical grade, including nickel chloride hexahydrate ($NiCl_2·6H_2O$, 99%), sodium molybdate dihydrate ($Na_2MoO_4·2H_2O$, 99%), hydrofluoric acid (HF; 48 wt%), potassium hydroxide (KOH; 98%), sulfuric acid (H_2SO_4, 98%), hydrazine hydrate ($N_2H_4·H_2O$, 80 wt%), anhydrous ethanol (CH_3CH_2OH, 99%), and tetramethylammonium hydroxide (TMAOH, 25 wt%), all of which were purchased from Sinopharm Chemical Reagent Co., Ltd. Selenium powder (Se, 99.9%) and Nafion solution (5 wt%) were purchased from Aladdin Reagent Co., Ltd. All purchased reagents were used as received without further purification. Deionized (DI) water with a resistivity of 18.2 MΩ·cm at room temperature was used in all experiments.

2.2 Synthesis of high-entropy M_4AlC_3

The detailed synthesis process of the high-entropy M_4AlC_3 phase has been reported in our previous work, and the specific chemical formula is $(Ti_{0.21}V_{0.21}Mo_{0.17}Nb_{0.22}Ta_{0.19})_4Al_{0.93}C_3$ [30]. Briefly, intermetallic compounds of Ti, V, Mo, Nb, Ta, and Al were first synthesized at 1100 °C. Subsequently, high-entropy carbides were obtained via a carbothermal reduction reaction at 1600 °C. Finally, the synthesized intermetallic compounds and high-entropy carbides were mixed and consolidated by spark plasma sintering (SPS-30T-20-III, Shanghai Chenhua Technology Co., Ltd.) at 1350 °C under a pressure of 50 MPa for 10 min. After cooling, the resulting product was crushed to obtain high-entropy M_4AlC_3 powder. The HAADF image, EDS elemental mapping, and selected area electron diffraction (SAED) pattern of M_4AlC_3, as shown in Fig. S1 in the Electronic Supplementary Material (ESM), confirm that Ti, V, Mo, Nb, and Ta are fully incorporated into a solid solution and that the M_4AlC_3 phase crystallizes in a standard hexagonal close-packed structure. Additionally, the final phase composition was determined to be 90.01 vol% M_4AlC_3, 2.98 vol% TaC and 7.01 vol% $MoAl_3$ through the Rietveld refinement method.

2.3 Synthesis of $M_4C_3T_x$ MXene nanosheets

High-entropy MXene $M_4C_3T_x$, with the chemical formula $(Ti_{0.21}V_{0.21}Mo_{0.17}Nb_{0.22}Ta_{0.19})_4C_3T_x$, was synthesized from self-fabricated high-entropy M_4AlC_3 powders via HF etching, as reported by Alhabeb *et al.* [31]. Specifically, 4.0 g of the high-entropy M_4AlC_3 powder was slowly added to 40 mL of 48 wt% HF aqueous solution. The reaction was stirred continuously at 60 °C for 72 h. After etching, the resulting black suspension was transferred into 50 mL centrifuge tubes and repeatedly washed with deionized water by centrifugation at 5000 r·min^{-1} for 5 min each cycle until the pH reached ≥ 6. The obtained product was then vacuum-filtered and vacuum-dried at 40 °C for 10 h to yield multilayer MXene, denoted as m-MXene.

Subsequently, 3 g of the multilayer MXene was mixed with 30 mL of TMAOH in a PTFE beaker and stirred at room temperature for 4 h. The mixture was then transferred into 50 mL centrifuge tubes, followed by the addition of absolute ethanol and centrifugation at 8000 r·min^{-1} for 5 min to discard the supernatant. Deionized water was added, and the mixture was centrifuged repeatedly at 6000 r·min^{-1} for 5 min per cycle until the pH reached ≤ 8. The final suspension was collected via vacuum-assisted filtration and freeze-dried to obtain single-to-few-layer MXene powders, denoted as f-MXene.

2.4 Synthesis of $MoSe_2/Ni_3Se_4/M_4C_3T_x$ MXene

A total of 4.67 mmol (0.369 g) of Se powder was mixed with 15 mL of $N_2H_4{\cdot}H_2O$ and stirred at room temperature for 2 h until the solution turned bright red. Meanwhile, 0.5 mmol (0.119 g) of $NiCl_2{\cdot}6H_2O$ and 2 mmol (0.484 g) of $Na_2MoO_4{\cdot}2H_2O$ were dissolved in 50 mL of deionized water. Subsequently, 25 mg of f-MXene was added to the above 50 mL solution, followed by the dropwise addition of 15 mL of the Se–$N_2H_4{\cdot}H_2O$ solution. The resulting mixture was ultrasonicated for 2 h, then transferred into a 100 mL stainless steel autoclave lined with PPL, and subjected to hydrothermal treatment at 220 °C for 20 h. After the reaction, the product was washed several times with anhydrous ethanol and deionized water to obtain the $MoSe_2/Ni_3Se_4/M_4C_3T_x$ MXene nanomaterial. For comparison, $MoSe_2$, $MoSe_2/Ni_3Se_4$, $MoSe_2/M_4C_3T_x$, and $Ni_3Se_4/M_4C_3T_x$ nanomaterials were also synthesized following the same procedure.

2.5 Characterizations

X-ray diffraction (XRD; Rigaku Ultima III, Japan) patterns of all samples were recorded using Cu-Kα radiation (50 kV, 40 mA) to determine the phase composition. Fourier transform infrared (FT-IR) spectra were measured using a spectrometer (Nicolet 6700, Thermo Scientific, USA) via the KBr pellet method. X-ray photoelectron spectroscopy (XPS; ESCALAB250, Thermo Scientific, USA) was employed to analyze the chemical states of the samples. The as-prepared f-MXene was first dispersed in deionized water to form a colloidal solution with a concentration of 1.0 mg·mL^{-1}. After ultrasonic treatment for 30 min, the dispersion was drop-cast onto Si wafers (for SEM and AFM) and copper grids (for TEM) for subsequent characterizations. Atomic force microscopy (AFM) images were obtained using a Fastscan instrument (Bruker, Germany). The morphology and structure of the nanomaterials were observed by scanning electron microscopy (SEM; JSM7800F, JEOL, Japan). High-magnification details were characterized using transmission electron microscopy (TEM; JEM 2100F, JEOL, Japan) equipped with an X-ray spectrometer (Octane Optima 60T, EDAX, USA).

2.6 Electrode preparation and electrochemical measurements

All electrochemical measurements were conducted using an electrochemical workstation (CHI 660e, Shanghai Chenhua Instrument Co., Ltd., China) in a standard three-electrode system. Typically, 4 mg of catalyst and 20 μL of Nafion solution were dispersed in 980 μL of a water/ethanol mixture (v/v = 1 : 1) and ultrasonicated for 30 min to form a homogeneous catalyst ink. Then, 5 μL of the ink (containing 20 μg of catalyst) was drop-cast onto the surface of a glassy carbon electrode with a diameter of 3 mm, resulting in a catalyst loading of 0.28 mg·cm^{-2}. In 0.5 M H_2SO_4 electrolyte, the catalyst-loaded glassy carbon electrode, an Ag/AgCl reference electrode (in 3 M KCl solution), and a platinum foil were used as the working electrode, reference electrode, and counter electrode, respectively. In 1 M KOH electrolyte, a Hg/HgO electrode and a graphite rod were used as the reference and counter electrodes, respectively. To compare the performance of different materials, polarization curves for HER were obtained by linear sweep voltammetry (LSV) at a scan rate of 10 mV·s^{-1}. In 0.5 M H_2SO_4 (pH = 1) and 1 M KOH (pH = 14) electrolytes, all measured potentials were converted to the reversible hydrogen electrode (RHE) scale according to Eqs. (1) and (2), respectively:

$$E_{RHE} = E_{Ag/AgCl} + 0.196V + 0.059\text{1pH} \quad (1)$$

$$E_{RHE} = E_{Hg/HgO} + 0.098V + 0.059\text{1pH} \quad (2)$$

where E_{RHE} is the electrode potential versus the reversible hydrogen electrode (RHE); $E_{Ag/AgCl}$ is the electrode potential relative to the Ag/AgCl reference electrode; $E_{Hg/HgO}$ is the electrode potential relative to the Hg/HgO reference electrode. V stands for volt.

The obtained potentials and voltages were all corrected with 90% iR compensation. The double-layer capacitance (C_{dl}) was calculated from cyclic voltammetry (C_V) tests at scan rates ranging from 20 to 120 mV·s^{-1}. Electrochemical impedance spectroscopy (EIS) was conducted over the frequency range of 0.01–10^5 Hz. To evaluate the stability of the $MoSe_2/Ni_3Se_4/M_4C_3T_x$ MXene catalyst, a 24-h chronoamperometry test was carried out.

2.7 Theoretical calculation

All first-principles calculations were carried out using the Vienna *ab initio* simulation package (VASP) based on density functional theory with the Perdew–Burke–Ernzerhof (PBE) functional within the generalized gradient approximation (GGA). To properly account for the weak interlayer interactions in the stacked MXene models, long-range dispersion interactions were included using the DFT-D method during structural optimization and electronic structure calculations. The plane-wave energy cutoff was set to 520 eV, and the Brillouin zone was sampled using a Γ-centered k-point mesh with a density of approximately 0.04 Å^{-1}. The electronic and ionic convergence criteria were set to 1.0×10^{-5} eV·atom^{-1} and 0.01 eV·Å^{-1}, respectively. The high-entropy phase $(Ti_{0.2}V_{0.2}Mo_{0.2}Nb_{0.2}Ta_{0.2})_4AlC_3$ was constructed using a 5 × 1 × 1 supercell, and the M-site atoms were randomly substituted via the special quasirandom structure (SQS) method implemented in the ATAT software package. To ensure comparability, V_4AlC_3, Nb_4AlC_3, and Ta_4AlC_3 were also modeled using supercells of the same 5 × 1 × 1 size. The resulting models were fully optimized and served as the basis for subsequent electronic structure calculations. To explore the intrinsic electronic properties of the carbide phases, Al atoms were removed from the relaxed M_4AlC_3 structures to generate $(Ti_{0.2}V_{0.2}Mo_{0.2}Nb_{0.2}Ta_{0.2})_4C_3$, V_4C_3, Nb_4C_3, and Ta_4C_3. Each model was further optimized with respect to cell volume and internal atomic positions to obtain the lowest-energy configuration, after which the total density of states (DOS) was computed. The surface termination groups T_x consist of 4 F atoms, 6 H atoms, and 16 O atoms. All termination groups are located in a hollow-site configuration on the surface M-layer metal atoms and are kept consistent across all systems. Figure S2 in the ESM shows the atomic structures of all the relevant models, including M_4AlC_3, M_4C_3, and $M_4C_3(F_{0.2}(OH)_{0.3}O_{0.5})_2$, as well as the corresponding V_4AlC_3, V_4C_3, $V_4C_3(F_{0.2}(OH)_{0.3}O_{0.5})_2$, Nb_4AlC_3, Nb_4C_3, $Nb_4C_3(F_{0.2}(OH)_{0.3}O_{0.5})_2$, Ta_4AlC_3, Ta_4C_3, and $Ta_4C_3(F_{0.2}(OH)_{0.3}O_{0.5})_2$. In addition, Fig. S3 in the ESM shows the Rietveld-refined XRD pattern of the experimentally obtained high-entropy M_4AlC_3, from which the lattice constants are determined to be a = 3.07 Å and c = 23.77 Å. In comparison, the lattice constants calculated for the M_4AlC_3 model constructed using the SQS method are a = 3.07 Å and c = 23.78 Å, showing excellent agreement. This close match validates the reliability of the constructed SQS model.

3 Results and discussion

3.1 Material characterizations

Figure 1 shows a schematic diagram of the synthesized nanohybrids. First, Al atoms in M_4AlC_3 crystals are selectively

removed using 48 wt% HF solution to prepare m-MXene. Then, the m-MXene powder is immersed in an aqueous TMAOH solution and stirred, allowing tetrabutylammonium (TMA) cations to intercalate, yielding f-MXene. Finally, using Se powder, $Na_2MoO_4{\cdot}2H_2O$, and $NiCl_2{\cdot}6H_2O$ as the Se, Mo, and Ni sources, respectively, $MoSe_2$ and Ni_3Se_4 nanoflowers are grown on the surface of the $M_4C_3T_x$ MXene matrix via a hydrothermal method, resulting in a $MoSe_2/Ni_3Se_4/M_4C_3T_x$ heterostructure. This approach not only effectively enhances the electronic conductivity of the electrocatalyst but also tunes its electronic structure, thus improving HER activity.

Figure 2 shows the XRD patterns of M_4AlC_3, m-MXene, and f-MXene. The diffraction peaks of M_4AlC_3 are significantly weakened, and the (002) diffraction peak shifts to a lower angle, indicating that the transformation from MAX to MXene has occurred [32]. Moreover, due to the successful intercalation of TMA cations, the interlayer spacing of f-MXene is further enlarged compared with m-MXene. In addition, the $MoAl_3$ phase, which exists as an impurity in the precursor material, is also removed by the HF solution during the etching process. The chemical structures of the samples were characterized by FT-IR spectroscopy (Fig. 2(c)). In M_4AlC_3, m-MXene, and f-MXene, characteristic absorption peaks are observed at approximately 3440–3460 and 1610–1620 cm^{-1}, corresponding to the presence of –OH bonds and C=O stretching vibrations, respectively. Compared with the MAX precursor, MXene additionally exhibits C–F stretching and O–H bending vibration peaks at 1140–1170 and 1390–1400 cm^{-1}, further confirming the introduction of –O, –F, and –OH terminal groups on the surface after etching and exfoliation treatment [29]. The SEM images of M_4AlC_3 and m-MXene are shown in Figs. 3(a) and 3(b), respectively. The former exhibits a stacked layered structure, while the latter displays a significantly increased interlayer spacing after etching. Figures 3(c) and 3(d) show the SEM and TEM images of f-MXene, respectively, revealing that the exfoliated f-MXene exhibits a sheet-like morphology. The inset in Fig. 3(c) displays the colloidal suspension of f-MXene obtained by centrifugation after intercalation with TMAOH. The HAADF image and EDS elemental mapping of f-MXene are shown in Fig. 3(e), indicating the uniform distribution of Ti, V, Mo, Nb, Ta, F, O, and C. No Al is detected, suggesting that Al is successfully removed. Figure 3(f) shows the high-resolution transmission electron microscopy (HRTEM) image of f-MXene, with the corresponding fast Fourier transform (FFT) pattern shown in the inset. The HRTEM image displays a periodic lattice structure of approximately 0.253 nm, corresponding to the (103) plane spacing of MXene, while the FFT pattern confirms the intrinsic hexagonal structure of MXene. In addition, the thickness of f-MXene is measured by AFM

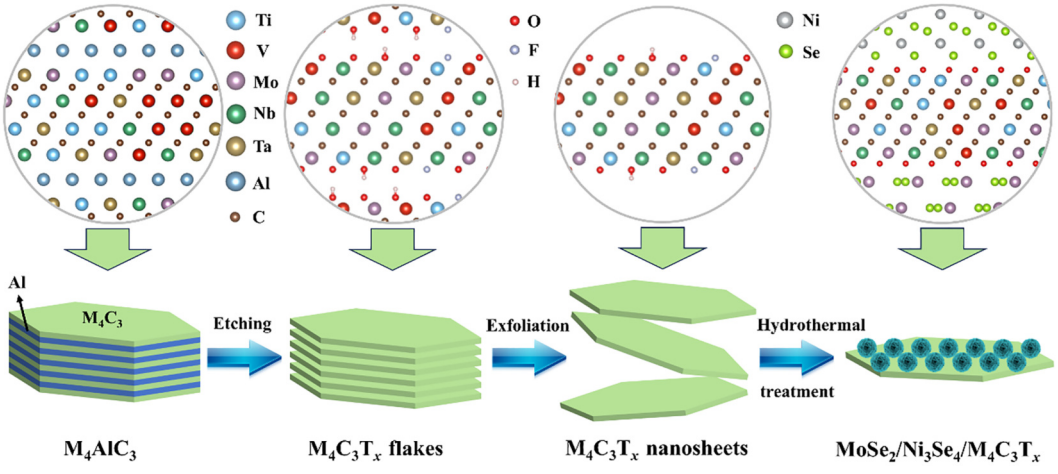

Fig. 1 Structural formulas and synthesis diagram of $MoSe_2/Ni_3Se_4/M_4C_3T_x$ nanohybrids.

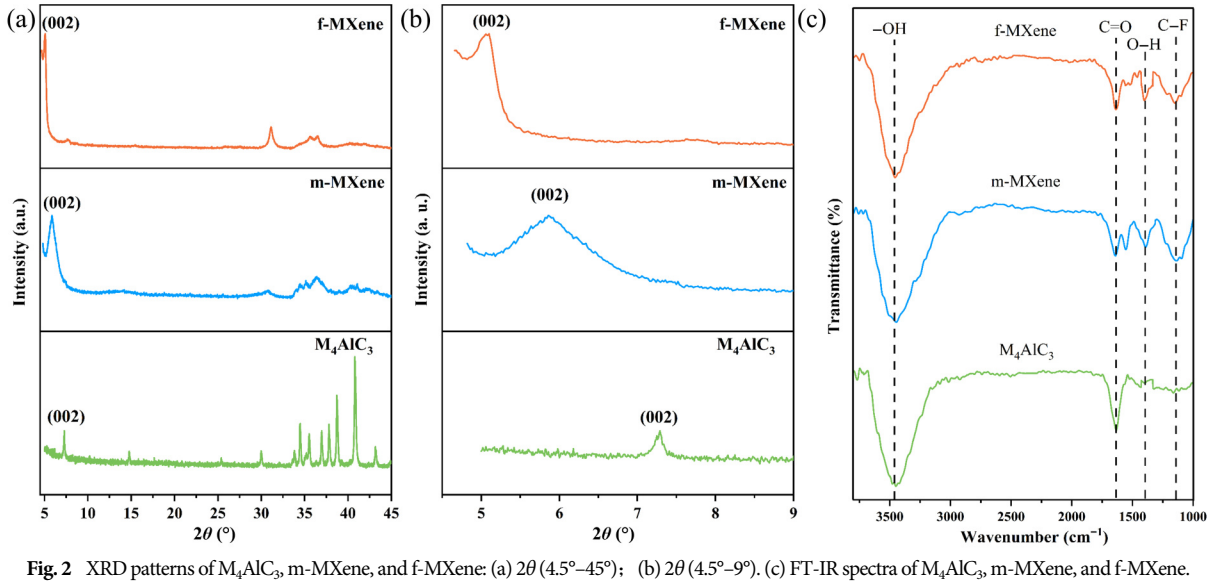

Fig. 2 XRD patterns of M_4AlC_3, m-MXene, and f-MXene: (a) 2θ (4.5°–45°); (b) 2θ (4.5°–9°). (c) FT-IR spectra of M_4AlC_3, m-MXene, and f-MXene.

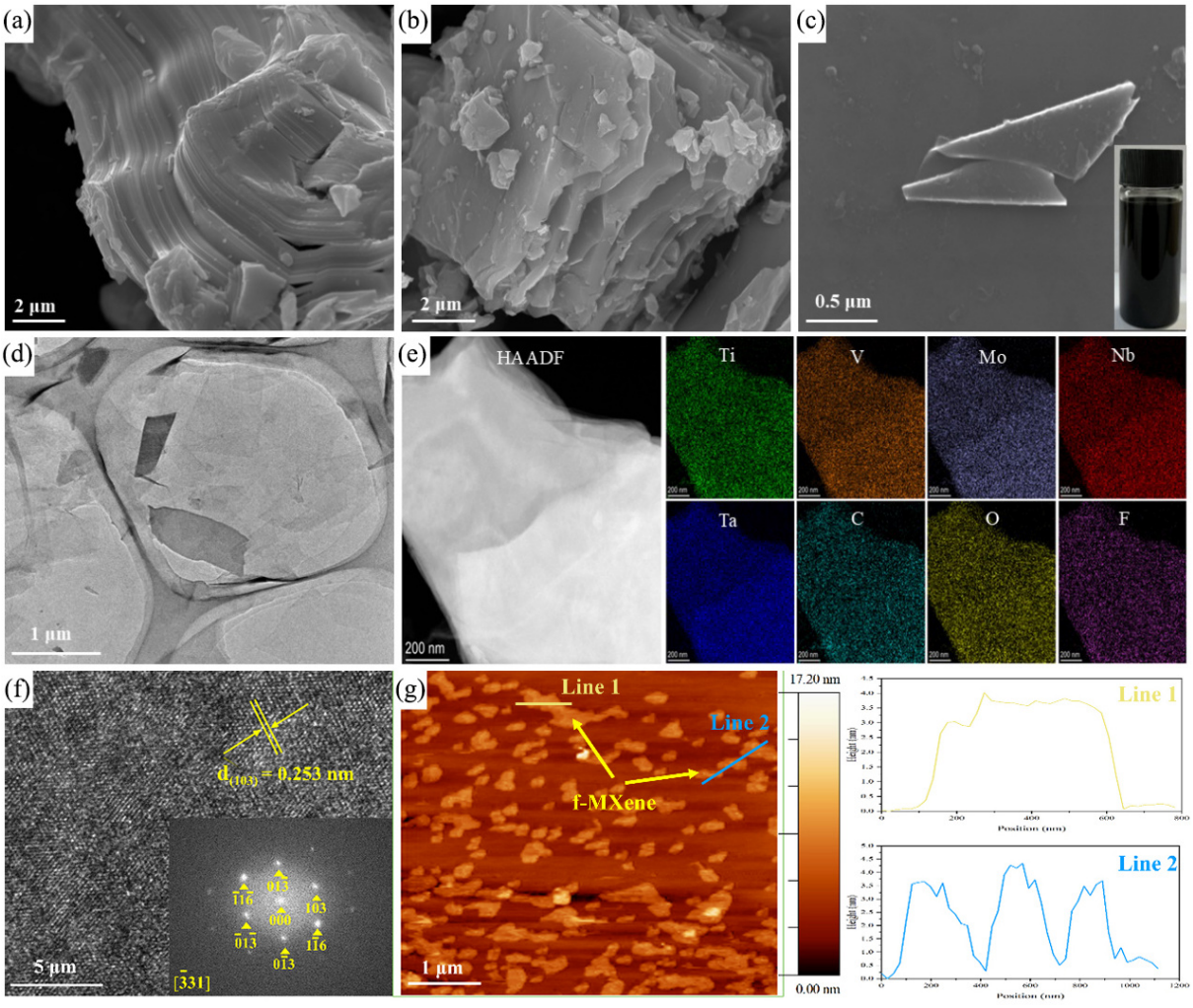

Fig. 3 (a) M_4AlC_3 SEM image; (b) m-MXene SEM image; (c)–(g) f-MXene morphology and structural characterization: (c) SEM image with inset showing the colloidal suspension, (d) TEM image, (e) HAADF image and EDS elemental mapping, (f) HRTEM image with FFT inset, and (g) AFM measurement of nanosheet thickness.

(Fig. 3(g)). The results show that the thickness of the f-MXene nanosheets ranges from approximately 3.5 to 4.5 nm.

The compositions of the high-entropy M_4AlC_3 phase and f-MXene are analyzed by XPS. The high-resolution spectra of Ti 2p, V 2p, Mo 3d, Nb 3d, Ta 4f, Al 2p, and C 1s for the high-entropy M_4AlC_3 phase, as well as Ti 2p, V 2p, Mo 3d, Nb 3d, Ta 4f, C 1s, F 1s, and O 1sfor f-MXene, are shown in Fig. 4 and Fig. S4 in the ESM, respectively, and summarized in Tables S1 and S2 in the ESM [25–28,33]. In the Ti 2p, V 2p, Mo 3d, Nb 3d, and Ta 4f regions, the main binding energy (BE) peaks of T_x–M–C species in f-MXene exhibit a positive shift of approximately 0.1–0.6 eV compared with the Al–M–C peaks in the high-entropy M_4AlC_3 phase. This shift is likely attributed to the replacement of Al by surface terminations, consistent with phenomena previously reported for Ti_2AlC, Ti_3AlC_2, $Ti_{1.0}V_{0.7}Cr_{0.05}Nb_{1.0}Ta_{1.0}AlC_3$ and their corresponding MXenes [28]. Moreover, the XPS survey spectrum further confirms that Al has been completely removed during the transformation of high-entropy M_4AlC_3 into MXene, while the emergence of F signals originates from HF treatment. Taken together, these results demonstrate that in 48 wt% HF solution, the relatively weakly bonded Al layers are selectively etched away, yielding MXene surfaces terminated with O, F, and OH groups. In addition, the chemical reactions that may occur during the etching of HE-MAX phases can be approximately described by simplified Eqs. (3)–(5):

$$M_4AlC_3 + 3HF = AlF_3 + 3/2H_2\uparrow + M_4C_3 \quad (3)$$

$$M_4C_3 + 2HF = H_2\uparrow + M_4C_3F_2 \quad (4)$$

$$M_4C_3 + 2H_2O = H_2\uparrow + M_4C_3(OH)_2 \quad (5)$$

Since Naguib *et al.* [34] first prepared $Ti_3C_2T_x$ MXene and proposed the relevant reaction equations in 2011, these simplified equations have been widely cited. However, in the actual reaction process, the actual functionalization process of the bare MX layer in water-soluble HF may be more complex than that shown in simplified Eqs. (2) and (3), and Eqs. (2) and (3) are likely to occur simultaneously and may be affected by factors such as solution concentration, temperature, and reaction time.

MXenes possess a large specific surface area due to their two-dimensional layered structure and generally exhibit high electrical conductivity. Neglecting scattering and other effects, this high conductivity can be verified by the large values measured near the Fermi level, as shown in Fig. 5. The results indicate that the electrical conductivity of high-entropy $M_4C_3(F_{0.2}(OH)_{0.3}O_{0.5})_2$ is significantly higher than that of $V_4C_3(F_{0.2}(OH)_{0.3}O_{0.5})_2$, $Nb_4C_3(F_{0.2}(OH)_{0.3}O_{0.5})_2$, and $Ta_4C_3(F_{0.2}(OH)_{0.3}O_{0.5})_2$. Therefore, the highly conductive high-entropy $M_4C_3T_x$ was used as a substrate to fabricate $MoSe_2/Ni_3Se_4/M_4C_3T_x$ nanomaterials.

The XRD patterns of $MoSe_2$, $MoSe_2/Ni_3Se_4$, $Ni_3Se_4/M_4C_3T_x$, $MoSe_2/M_4C_3T_x$, and $MoSe_2/Ni_3Se_4/M_4C_3T_x$ nanomaterials are

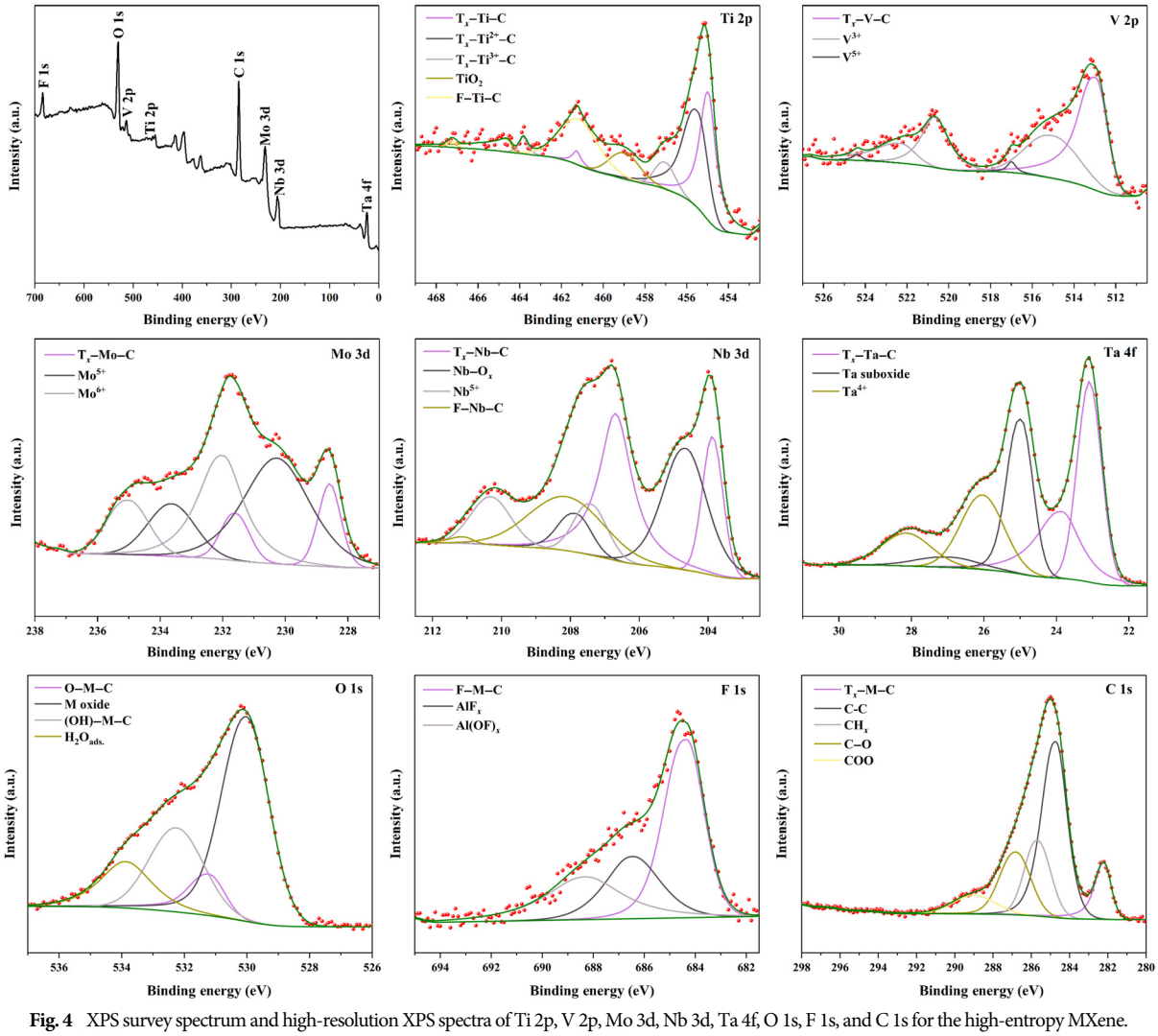

Fig. 4 XPS survey spectrum and high-resolution XPS spectra of Ti 2p, V 2p, Mo 3d, Nb 3d, Ta 4f, O 1s, F 1s, and C 1s for the high-entropy MXene.

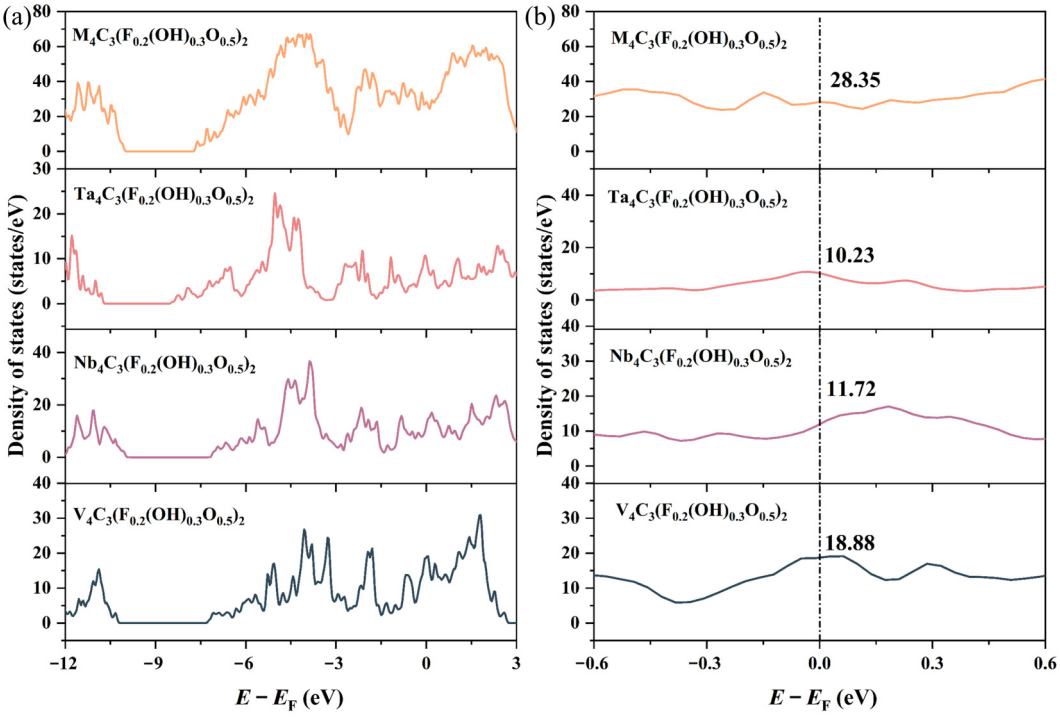

Fig. 5 Total electronic density of states (TDOS) curves of $M_4C_3(F_{0.2}(OH)_{0.3}O_{0.5})_2$, $V_4C_3(F_{0.2}(OH)_{0.3}O_{0.5})_2$, $Nb_4C_3(F_{0.2}(OH)_{0.3}O_{0.5})_2$, and $Ta_4C_3(F_{0.2}(OH)_{0.3}O_{0.5})_2$: (a) E–E_F: −12–3; (b) E–E_F: −0.6–0.6.

shown in Fig. 6. All the results exhibit the characteristic diffraction peaks of $MoSe_2$ (JCPDS No. 29-0914) and/or Ni_3Se_4 (JCPDS No. 18-0890). Compared with $Ni_3Se_4/M_4C_3T_x$, the diffraction peaks of Ni_3Se_4 in $MoSe_2/Ni_3Se_4$ and $MoSe_2/Ni_3Se_4/M_4C_3T_x$ shift toward lower angles, which may be attributed to the partial solid solution of Mo in the Ni_3Se_4 crystal structure. In addition, compared with f-MXene, the (002) peak of f-MXene in $Ni_3Se_4/M_4C_3T_x$, $MoSe_2/M_4C_3T_x$, and $MoSe_2/Ni_3Se_4/M_4C_3T_x$ shifts toward higher angles (from 5.1° to 6.1°), corresponding to a contraction of the interlayer spacing. This phenomenon can be ascribed to two synergistic factors: (i) dehydration of interlayer water under hydrothermal conditions, and (ii) the $MoSe_2$ and Ni_3Se_4 nanosheets forming a densely packed structure confined between the MXene layers, and this three-dimensional spatial confinement effectively suppresses the re-expansion of MXene layers after the hydrothermal process. Meanwhile, the interfacial interactions between the heterostructure components and the MXene substrate further stabilize the contracted interlayer configuration.

Figures S5(a)–S5(d) in the ESM show the SEM images of $MoSe_2$, $MoSe_2/Ni_3Se_4$, $Ni_3Se_4/M_4C_3T_x$, and $MoSe_2/M_4C_3T_x$, respectively, while the SEM image of $MoSe_2/Ni_3Se_4/M_4C_3T_x$ is presented in Fig. 7(a). The petal-like $MoSe_2$ nanomaterials exhibit sizes of several tens of nanometers, whereas the incorporation of Ni_3Se_4 renders the $MoSe_2$ nanoflowers more disordered. Moreover, the $MoSe_2$ and/or Ni_3Se_4 nanomaterials encapsulate f-MXene and fill the interlayer spaces of f-MXene. TEM characterization is employed to further confirm the formation of the heterostructure, as shown in Fig. 7 and Fig. S6 in the ESM. For $MoSe_2$ (Figs. S6(a)–S6(d) in the ESM), the TEM image reveals a typical petal-like structure assembled from randomly distributed nanosheets, which is consistent with the SEM results. The HRTEM image displays lattice fringes with periodic spacings of approximately 0.237 and 0.285 nm, corresponding to the (103) plane of 1T $MoSe_2$ and the (100) plane of 2H $MoSe_2$, respectively. This indicates the coexistence of both 1T and 2H phases in the as-prepared $MoSe_2$, as frequently reported in previous studies. Meanwhile, the homogeneous distribution of Mo and Se in the HAADF image and EDS mapping further confirms the compositional uniformity of $MoSe_2$. For $MoSe_2/Ni_3Se_4$ (Figs. S6(e) and S6(f) in the ESM), the TEM image exhibits a more complex two-dimensional interlaced structure compared with single-phase $MoSe_2$, and the HAADF image together with the EDS mapping demonstrates the uniform distribution of Ni, Mo, and Se, indicating the successful construction of the binary heterostructure. For $Ni_3Se_4/M_4C_3T_x$ (Figs. S6(g) and S6(h) in the ESM) and $MoSe_2/M_4C_3T_x$ (Figs. S6(i)–S6(k) in the ESM), the TEM images display tightly integrated morphologies of Ni_3Se_4 and $MoSe_2$ nanostructures with $M_4C_3T_x$, respectively. Correspondingly, the EDS mapping results show that Ni and Se in the former, as well as Mo and Se in the latter, are spatially consistent with the characteristic elements of $M_4C_3T_x$ (Ti, V, Mo, Nb, Ta, C). In the ternary $MoSe_2/Ni_3Se_4/M_4C_3T_x$ system (Fig. 7), TEM images clearly reveal that the Ni_3Se_4 and $MoSe_2$ nanomaterials are tightly attached to the surface of $M_4C_3T_x$, exhibiting a stable composite morphology. HRTEM images display lattice fringes with periodic spacings of approximately 0.697, 0.306, and 0.297 nm, corresponding to the d - spacings of the (002) plane of $MoSe_2$, the (-103) plane of Ni_3Se_4, and the (008) plane of $M_4C_3T_x$, respectively, directly confirming the coexistence of the three phases. Meanwhile, HAADF images and EDS elemental mapping indicate that Ti, V, Mo, Nb, Ta, C, Ni, and Se are uniformly distributed in the loaded regions. Collectively, these results systematically verify the successful fabrication of the $MoSe_2$, $MoSe_2/Ni_3Se_4$, $Ni_3Se_4/M_4C_3T_x$, $MoSe_2/M_4C_3T_x$, and $MoSe_2/Ni_3Se_4/M_4C_3T_x$ nanomaterials.

The chemical states of the prepared $MoSe_2/Ni_3Se_4/M_4C_3T_x$ nanomaterials were analyzed by XPS, as shown in Fig. 8 and summarized in Table S3 in the ESM. Compared with f-MXene, the survey spectrum (Fig. 8(a)) of the heterostructure reveals the newly detected Se and Ni. In addition, as the signals of Ti 2p, V 2p, Nb 3d, and Ta 4f in the heterostructure are very weak, no curve fitting was performed. The XPS spectrum of Mo 3d (Fig. 8(b))

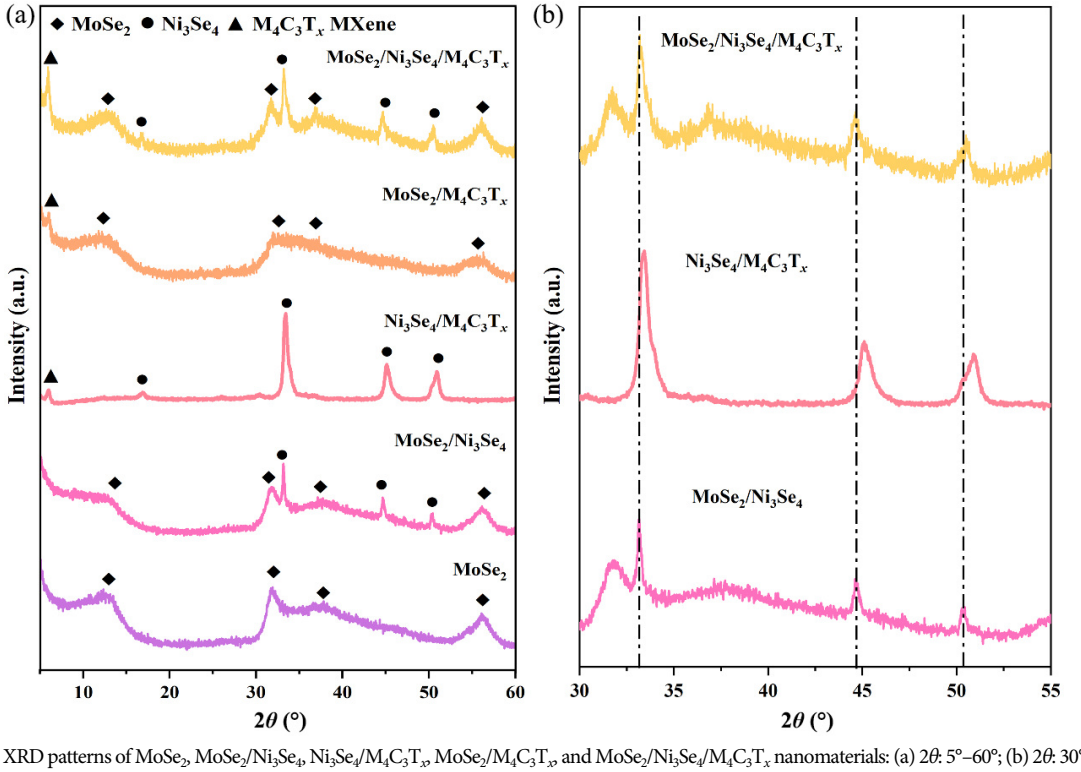

Fig. 6 XRD patterns of $MoSe_2$, $MoSe_2/Ni_3Se_4$, $Ni_3Se_4/M_4C_3T_x$, $MoSe_2/M_4C_3T_x$, and $MoSe_2/Ni_3Se_4/M_4C_3T_x$ nanomaterials: (a) 2θ: 5°–60°; (b) 2θ: 30°–55°.

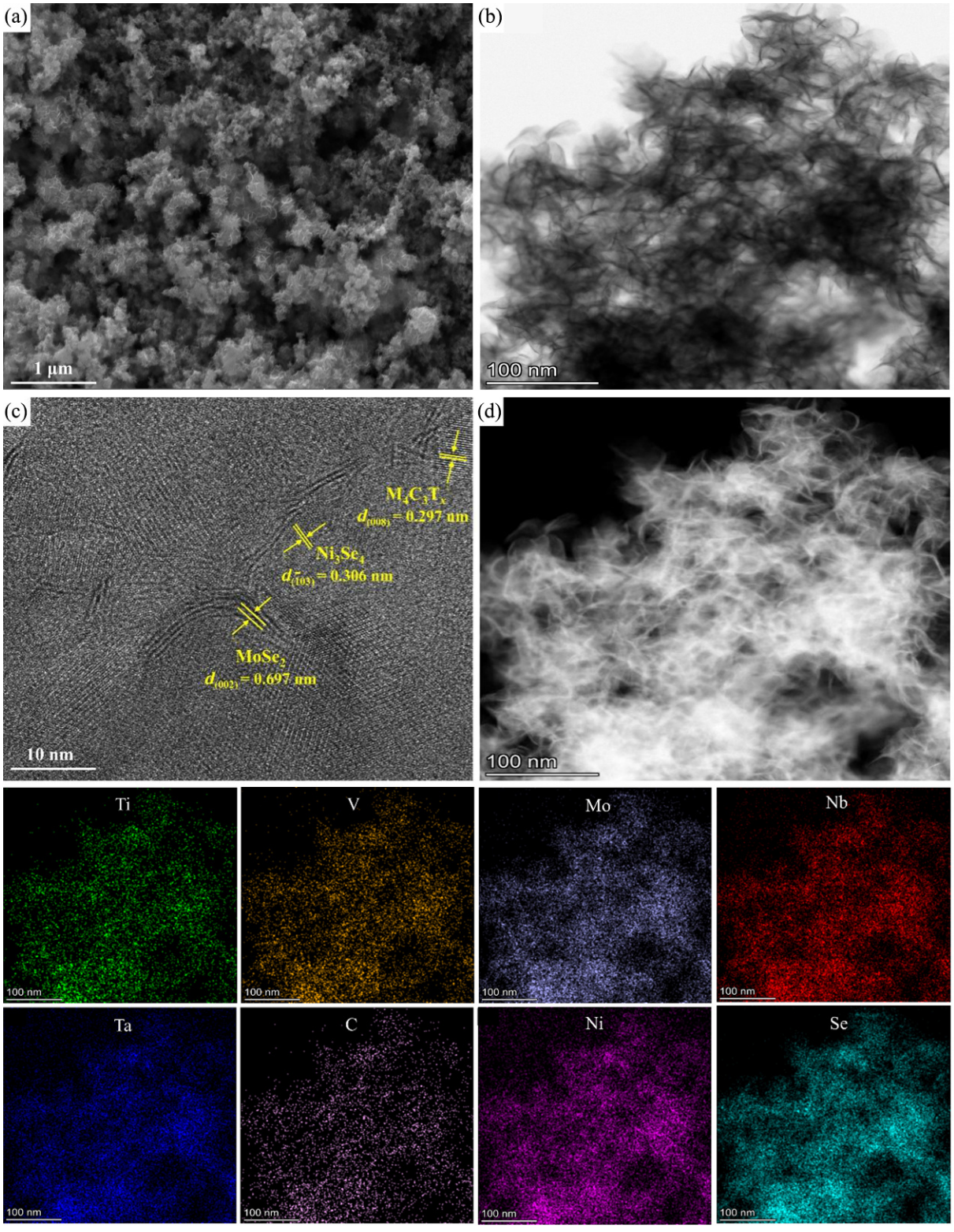

Fig. 7 (a) SEM image; (b) TEM image; (c) HRTEM image and (d) HAADF image and EDS elemental mappings of the $MoSe_2/Ni_3Se_4/M_4C_3T_x$ nanomaterial.

can be deconvoluted into 10 peaks; in addition to the six intrinsic peaks of f-MXene, four new peaks are observed: 229.0 and 232.1 eV corresponding to 2H-phase $MoSe_2$ and 228.8 and 231.8 eV corresponding to 1T-phase $MoSe_2$. In the Ni 2p spectrum (Fig. 8(c)), the peaks at 853.3 and 870.4 eV correspond to Ni^{2+} $2p_{3/2}$ and Ni^{2+} $2p_{1/2}$, while the peaks at 855.4 and 872.0 eV correspond to Ni^{3+} $2p_{3/2}$ and Ni^{3+} $2p_{1/2}$. Meanwhile, two high-binding-energy satellite peaks are also detected at 860.8 and 877.2 eV, corresponding to Ni $2p_{3/2}$ and Ni $2p_{1/2}$. The Se 3d spectrum (Fig. 8(d)) shows peaks at 54.2 and 54.8 eV, which correspond to Se $3d_5/_2$ and Se $3d_{3/2}$ orbitals, indicating a −2 valence state of Se. After deconvolution, the peaks at 53.9 and 54.9 eV are attributed to 1T-phase $MoSe_2$, while those at 54.3 and 55.2 eV correspond to 2H-phase $MoSe_2$. In addition, the peak located at 59.0 eV suggests the surface oxidation state of Se species [19,35–37]. The O 1s XPS region (Fig. 8(e)) can be fitted into two

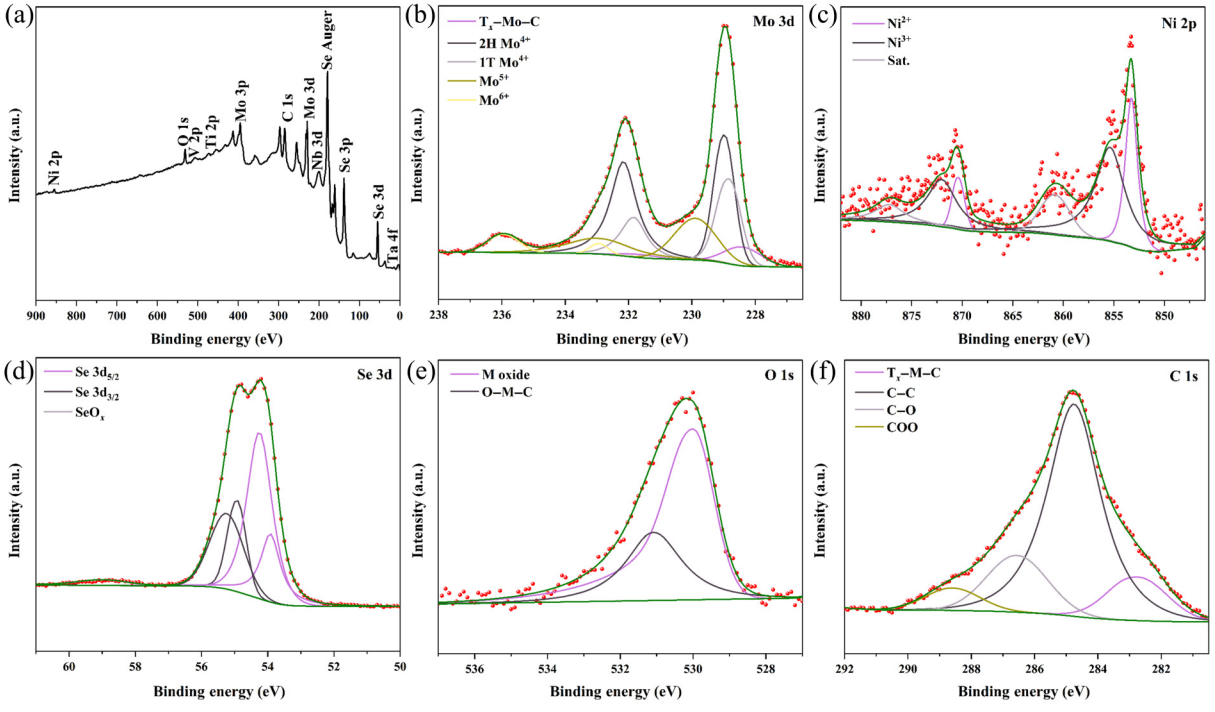

Fig. 8 XPS survey spectrum and high-resolution XPS spectra of Mo 3d, Ni 2p, Se 3d, O 1s and C 1s for $MoSe_2/Ni_3Se_4/M_4C_3T_x$.

peaks at 530.0 and 531.1 eV, corresponding to metal oxides and O–M–C bonds, respectively. The C 1s XPS region (Fig. 8(f)) can be deconvoluted into four peaks at 282.7, 284.8, 286.6, and 288.6 eV, assigned to T_x–M–C, C–C, C–O, and COO bonds, respectively.

3.2 Electrochemical characterizations

3.2.1 HER activities in 0.5 M H_2SO_4

In a typical three-electrode system with 0.5 M H_2SO_4 as the electrolyte, the HER catalytic performances of Pt/C, M_4AlC_3, f-MXene, $MoSe_2$, $MoSe_2/Ni_3Se_4$, $Ni_3Se_4/M_4C_3T_x$, $MoSe_2/M_4C_3T_x$, and $MoSe_2/Ni_3Se_4/M_4C_3T_x$ electrocatalysts are evaluated. First, the HER catalytic activities of all catalysts are tested by linear sweep voltammetry (LSV), as shown in Fig. 9(a). It can be observed that $MoSe_2/Ni_3Se_4/M_4C_3T_x$ exhibits excellent HER activity, second only to commercial Pt/C (20 wt% Pt loading). For a given current density, the overpotential is inversely correlated with the catalytic performance. Figure 9(b) presents the overpotentials at a current density of 10 mA·cm^{-2}. The overpotential of $MoSe_2/Ni_3Se_4/M_4C_3T_x$ is only 67 mV, which is significantly lower than that of $MoSe_2/M_4C_3T_x$ (91 mV), $MoSe_2/Ni_3Se_4$ (117 mV), $Ni_3Se_4/M_4C_3T_x$ (153 mV), f-MXene (205 mV), $MoSe_2$ (222 mV), and M_4AlC_3 (455 mV) and slightly higher than that of commercial Pt/C (34 mV). The smaller overpotential indicates that $MoSe_2/Ni_3Se_4/M_4C_3T_x$ possesses superior catalytic activity for the HER. Compared with other materials, this material exhibits a lower overpotential (Table S4 in the ESM), indicating a faster hydrogen evolution rate [38–49]. The Tafel slope is obtained by fitting the LSV curves to evaluate the HER kinetics of the catalysts, as shown in Fig. 9(c). A smaller Tafel slope indicates faster catalytic kinetics. The Tafel slope of $MoSe_2/Ni_3Se_4/M_4C_3T_x$ is 68.7 mV·dec^{-1}, which is larger than that of Pt/C (37.8 mV·dec^{-1}) but smaller than those of $MoSe_2/M_4C_3T_x$ (76.3 mV·dec^{-1}), $MoSe_2/Ni_3Se_4$ (94.9 mV·dec^{-1}), $Ni_3Se_4/M_4C_3T_x$ (86.1 mV·dec^{-1}), f-MXene (116.2 mV·dec^{-1}), and $MoSe_2$ (74.1 mV·dec^{-1}). The smaller Tafel slope of $MoSe_2/Ni_3Se_4/M_4C_3T_x$ confirms its faster HER kinetics. Furthermore, the study of Tafel slopes can provide insights into the mechanism of the HER. Typically, different rate-determining steps correspond to characteristic Tafel slopes: when the Volmer step is rate-limiting, the slope is approximately 120 mV·dec^{-1}; when the Heyrovsky step dominates, it is approximately 40 mV·dec^{-1}; and when the Tafel step is rate-determining, the slope is approximately 30 mV·dec^{-1}. The experimental results indicate that the Tafel slope of $MoSe_2/Ni_3Se_4/M_4C_3T_x$ lies between 120 and 40 mV·dec^{-1}, suggesting that the HER follows a Volmer–Heyrovsky mechanism. In this mechanism, M represents the catalyst, e^- denotes an electron, and M–H corresponds to a hydrogen atom adsorbed on the catalyst surface. The reaction steps can be described as Reactions (6) and (7) [50]:

$$\text{Volmer step}: H_3O^+ + e^- \rightarrow M - H + H_2O \quad (6)$$

$$\text{Heyrovsky step}: H_3O^+ + e^- + M - H \rightarrow H_2 + M + H_2O \quad (7)$$

The electronic transport kinetics of the catalysts were further evaluated using electrochemical impedance spectroscopy (EIS), as shown in Fig. 9(d). The inset depicts the equivalent circuit model employed, where Rs represents the solution resistance, R_{ct} denotes the charge-transfer resistance, and CPE corresponds to the constant phase element. The results indicate that $MoSe_2/Ni_3Se_4/M_4C_3T_x$ exhibits the lowest R_{ct}, suggesting the fastest electron transport, which confirms that constructing a heterostructure facilitates enhanced electron transfer. The HER activity is closely related to the electrochemically active surface area (ECSA) of the catalyst, which can be inferred from the electrochemical double-layer capacitance (C_{dl}). The C_{dl} values of the catalysts (Fig. 9(f)) were obtained from cyclic voltammetry (C_V) measurements performed in the nonfaradaic region (−0.3 to −0.2 V vs. RHE) at various scan rates (20, 40, 60, 80, 100, and 120 mV·s^{-1}) (Fig. 9(e) and Figs. S7(a)–S7(e) in the ESM). The results show that $MoSe_2/Ni_3Se_4/M_4C_3T_x$ has C_{dl} of 115.7 mF·cm^{-2}, which is significantly higher than those of $MoSe_2/M_4C_3T_x$ (62.1 mF·cm^{-2}), $MoSe_2/Ni_3Se_4$ (46.6 mF·cm^{-2}), $Ni_3Se_4/M_4C_3T_x$ (25.6 mF·cm^{-2}), f-MXene (10.1 mF·cm^{-2}), and $MoSe_2$ (12.3 mF·cm^{-2}).

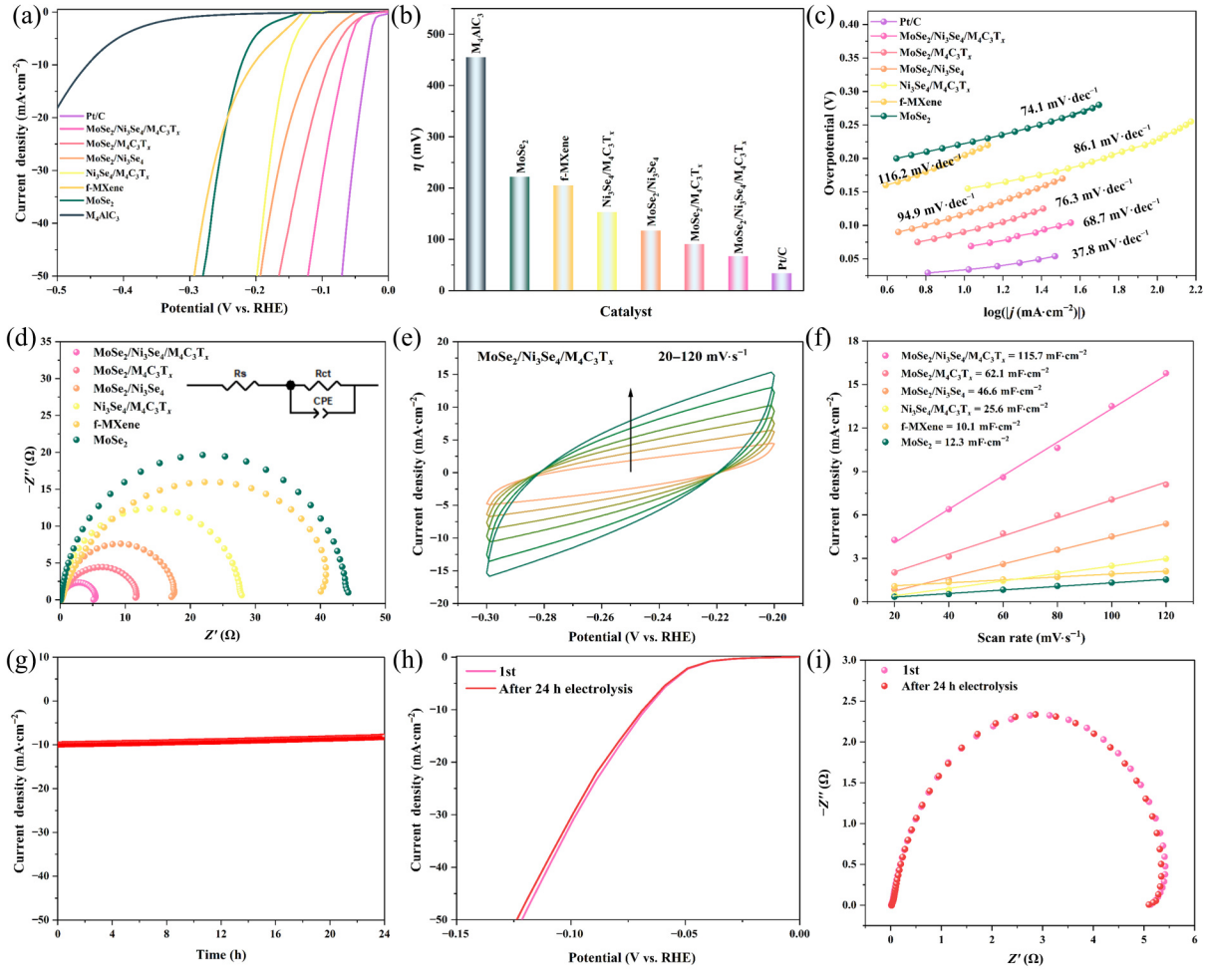

Fig. 9 (a) LSV curves of Pt/C, M_4AlC_3, f-MXene, $MoSe_2$, $MoSe_2/Ni_3Se_4$, $Ni_3Se_4/M_4C_3T_x$, $MoSe_2/M_4C_3T_x$, and $MoSe_2/Ni_3Se_4/M_4C_3T_x$ in 0.5 M H_2SO_4 toward the HER. (b) Overpotentials of different materials at 10 mA·cm^{-2} current density. (c) Tafel plots of HER performance evolved from (a). (d) Nyquist plots of f-MXene, $MoSe_2$, $MoSe_2/Ni_3Se_4$, $Ni_3Se_4/M_4C_3T_x$, $MoSe_2/M_4C_3T_x$, and $MoSe_2/Ni_3Se_4/M_4C_3T_x$. (e) Cyclic voltammograms for $MoSe_2/Ni_3Se_4/M_4C_3T_x$ at different rates ranging from 20 to 120 mV·s^{-1} in the region from −0.3 to −0.2 V. (f) Estimated C_{dl} values of f-MXene, $MoSe_2$, $MoSe_2/Ni_3Se_4$, $Ni_3Se_4/M_4C_3T_x$, $MoSe_2/M_4C_3T_x$, and $MoSe_2/Ni_3Se_4/M_4C_3T_x$. (g) $MoSe_2/Ni_3Se_4/M_4C_3T_x$ chronoamperometric response at 10 mA·cm^{-2} (0.5 M H_2SO_4). (h) LSV curves and (i) Nyquist plots collected before and after 24 h of electrolysis.

Since the ECSA is directly proportional to C_{dl}, a larger C_{dl} indicates a higher ECSA, demonstrating that $MoSe_2/Ni_3Se_4/M_4C_3T_x$ possesses the largest electrochemically active surface area among the tested catalysts.

Long-term stability is another important indicator for evaluating catalytic performance. As shown in Fig. 9(g), the chronoamperometry (*i*–*t*) curve demonstrates that the current density remains nearly unchanged during the 24 h test. Fig. 9(h) and Fig. 9(i) present the LSV curves and Rct values of $MoSe_2/Ni_3Se_4/M_4C_3T_x$ before and after the i–t experiment, respectively, and the results show that they are almost identical, indicating the excellent HER catalytic stability of $MoSe_2/Ni_3Se_4/M_4C_3T_x$ in 0.5 M H_2SO_4.

3.2.2 *HER activities in 1.0 M KOH*

The HER performance of the catalysts under alkaline conditions was evaluated using 1.0 M KOH as the electrolyte. The LSV curves are shown in Fig. 10(a). It can be observed that $MoSe_2/Ni_3Se_4/M_4C_3T_x$ also exhibits excellent HER activity in 1.0 M KOH, second only to commercial Pt/C. Figure 10(b) presents the overpotentials at a current density of 10 mA·cm^{-2}. The overpotential of $MoSe_2/Ni_3Se_4/M_4C_3T_x$ is only 73 mV, which is significantly lower than those of $MoSe_2/M_4C_3T_x$ (192 mV), $MoSe_2/Ni_3Se_4$ (284 mV), $Ni_3Se_4/M_4C_3T_x$ (336 mV), f-MXene (382 mV), $MoSe_2$ (355 mV), and M_4AlC_3 (760 mV) and only slightly higher than that of commercial Pt/C (42 mV). The smaller overpotential indicates that $MoSe_2/Ni_3Se_4/M_4C_3T_x$ possesses superior HER catalytic activity in 1.0 M KOH. The corresponding Tafel slopes are shown in Fig. 10(c). The Tafel slope of $MoSe_2/Ni_3Se_4/M_4C_3T_x$ is 77.8 mV·dec^{-1}, higher than that of Pt/C (43.3 mV·dec^{-1}) but lower than those of $MoSe_2/M_4C_3T_x$ (101.2 mV·dec^{-1}), $MoSe_2/Ni_3Se_4$ (127.4 mV·dec^{-1}), $Ni_3Se_4/M_4C_3T_x$ (125.7 mV·dec^{-1}), f-MXene (167.9 mV·dec^{-1}), and $MoSe_2$ (156.1 mV·dec^{-1}). The smaller Tafel slope confirms that $MoSe_2/Ni_3Se_4/M_4C_3T_x$ exhibits faster HER kinetics in 1.0 M KOH. Since the Tafel slope lies between 120 and 40 mV·dec^{-1}, the HER process in 1.0 M KOH follows the Volmer–Heyrovsky mechanism. Table S4 in the ESM compares the electrocatalytic performance of $MoSe_2/Ni_3Se_4/M_4C_3T_x$ under alkaline conditions with that of reported HER electrocatalysts, showing its high catalytic efficiency.

The collected Nyquist plots are shown in Fig. 10(d), where $MoSe_2/Ni_3Se_4/M_4C_3T_x$ displays the lowest Rct, indicating the fastest electron transfer rate in 1.0 M KOH. The C_{dl} values of the catalysts in 1.0 M KOH (Fig. 10(f)) were determined from CV measurements conducted in the nonfaradaic region (−0.4 to −0.3 V vs. RHE) at different scan rates (20, 40, 60, 80, 100, and 120 mV·s^{-1}) (Fig. 10(e) and Figs. S8(a)–S8(e)). The results show

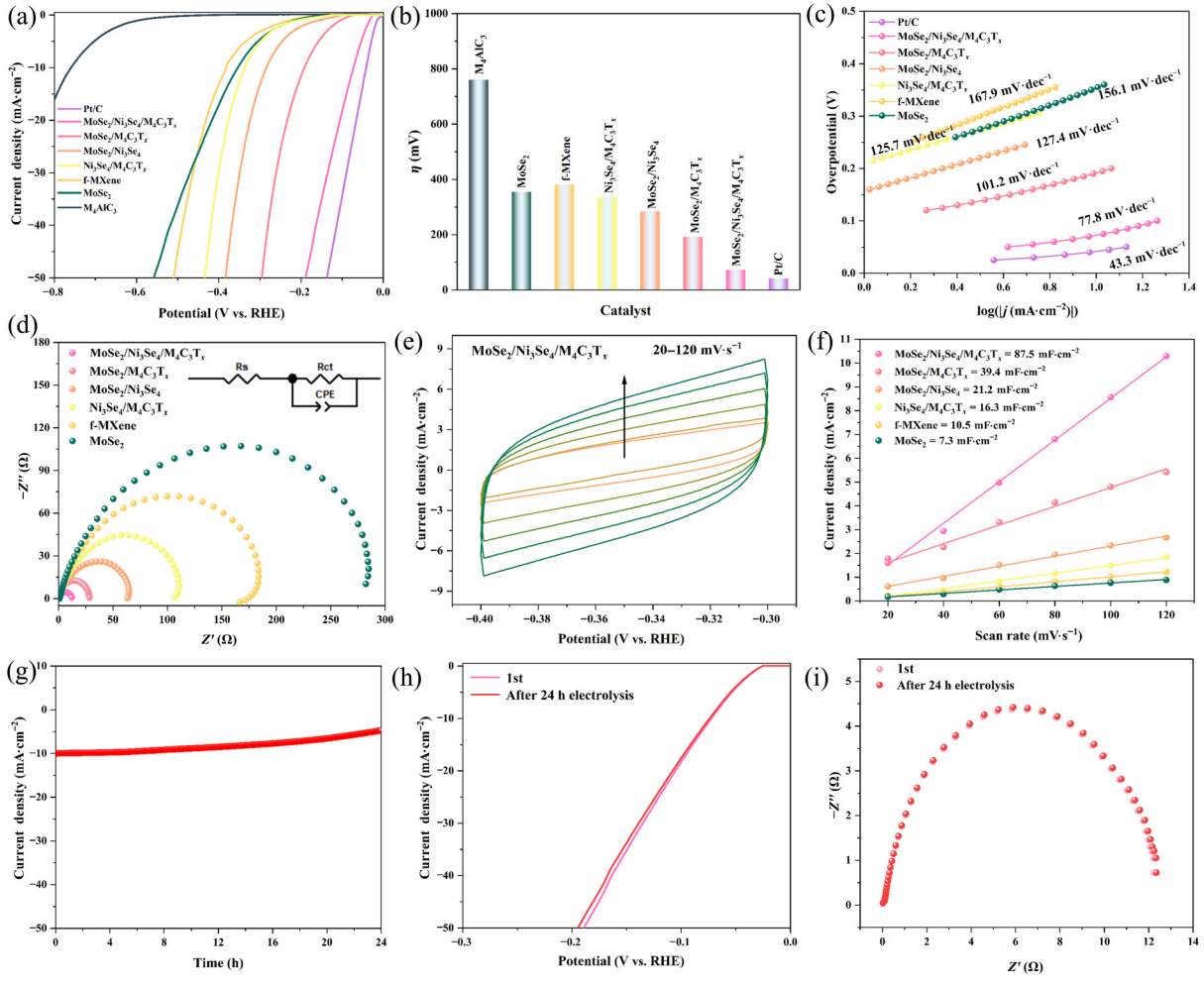

Fig. 10 (a) LSV curves of Pt/C, M_4AlC_3, f-MXene, $MoSe_2$, $MoSe_2/Ni_3Se_4$, $Ni_3Se_4/M_4C_3T_x$, $MoSe_2/M_4C_3T_x$, and $MoSe_2/Ni_3Se_4/M_4C_3T_x$ in 1.0 M KOH toward the HER. (b) Overpotentials of different materials at 10 mA·cm^{-2} current density. (c) Tafel plots of HER performance evolved from (a). (d) Nyquist plots of f-MXene, $MoSe_2$, $MoSe_2/Ni_3Se_4$, $Ni_3Se_4/M_4C_3T_x$, $MoSe_2/M_4C_3T_x$, and $MoSe_2/Ni_3Se_4/M_4C_3T_x$. (e) Cyclic voltammograms for $MoSe_2/Ni_3Se_4/M_4C_3T_x$ at different rates ranging from 20 to 120 mV·s^{-1} in the region from −0.4 to −0.3 V. (f) Estimated C_{dl} values of f-MXene, $MoSe_2$, $MoSe_2/Ni_3Se_4$, $Ni_3Se_4/M_4C_3T_x$, $MoSe_2/M_4C_3T_x$, and $MoSe_2/Ni_3Se_4/M_4C_3T_x$. (g) $MoSe_2/Ni_3Se_4/M_4C_3T_x$ chronoamperometric response at 10 mA·cm^{-2} (1.0 M KOH). (h) LSV curves and (i) Nyquist plots collected before and after 24 h of electrolysis.

that $MoSe_2/Ni_3Se_4/M_4C_3T_x$ has a C_{dl} of 87.5 mF·cm^{-2}, which is much higher than those of $MoSe_2/M_4C_3T_x$ (39.4 mF·cm^{-2}), $MoSe_2/Ni_3Se_4$ (21.2 mF·cm^{-2}), $Ni_3Se_4/M_4C_3T_x$ (16.3 mF·cm^{-2}), f-MXene (10.5 mF·cm^{-2}), and $MoSe_2$ (7.3 mF·cm^{-2}). This indicates that $MoSe_2/Ni_3Se_4/M_4C_3T_x$ possesses the largest electrochemically active surface area.

The *i–t* curve in 1.0 M KOH is shown in Fig. 10(g), where only minor fluctuations in current density are observed during the 24 h test. Fig. 10(h) and Fig. 10(i) present the LSV curves and R_{ct} values of $MoSe_2/Ni_3Se_4/M_4C_3T_x$ before and after the *i–t* experiment in 1.0 M KOH, respectively, and the results remain nearly identical, demonstrating the excellent HER catalytic stability of this material in 1.0 M KOH. To evaluate the stability of $MoSe_2/Ni_3Se_4/M_4C_3T_x$, the catalysts after 24 h of testing in 1 M KOH and 0.5 M H_2SO_4 were characterized. As shown in Fig. 11(a), the XRD pattern exhibits almost no change compared with the initial sample, indicating that $MoSe_2/Ni_3Se_4/M_4C_3T_x$ maintains excellent compositional stability during the HER process. The SEM images in Figs. 11(b) and 11(d) and the TEM images in Figs. 11(c) and 11(e) show that $MoSe_2/Ni_3Se_4$ remains uniformly anchored on the $M_4C_3T_x$ MXene nanosheets, confirming the morphological stability of $MoSe_2/Ni_3Se_4/M_4C_3T_x$ during the HER. The excellent structural stability of the material can be attributed to the synergistic effect of a multilevel interfacial stabilization mechanism. First, the abundant functional groups on the surface of the high-entropy MXene provide effective anchoring sites for the metal precursors, guiding the *in situ* epitaxial growth of $MoSe_2$ and Ni_3Se_4 nanosheets on its surface and within the layers to form a stable multidimensional composite structure. This structure not only includes 2D/2D stacked interfaces but also exhibits a composite feature of a 2D substrate with 3D nanoflowers. Second, the uniformly dispersed heterojunction nanosheets, orderly arranged within and on the surface of the MXene layers, create a unique spatial confinement effect that significantly reduces the surface mobility of active species, thereby mitigating potential Ostwald ripening during long-term operation. In addition, the intrinsically excellent structural stability and mechanical strength of the high-entropy MXene substrate provide a robust supporting framework for the entire heterostructure system, and the retention of the microstructure after reaction further validates the rationality of this unique structural design. In summary, $MoSe_2/Ni_3Se_4/M_4C_3T_x$ demonstrates outstanding structural and performance stability, making it a highly promising HER catalyst candidate in both acidic and alkaline media.

3.2.3 *HER mechanism analysis*

The $MoSe_2/Ni_3Se_4/M_4C_3T_x$ electrocatalyst exhibits outstanding HER activity in both acidic and alkaline environments, which is

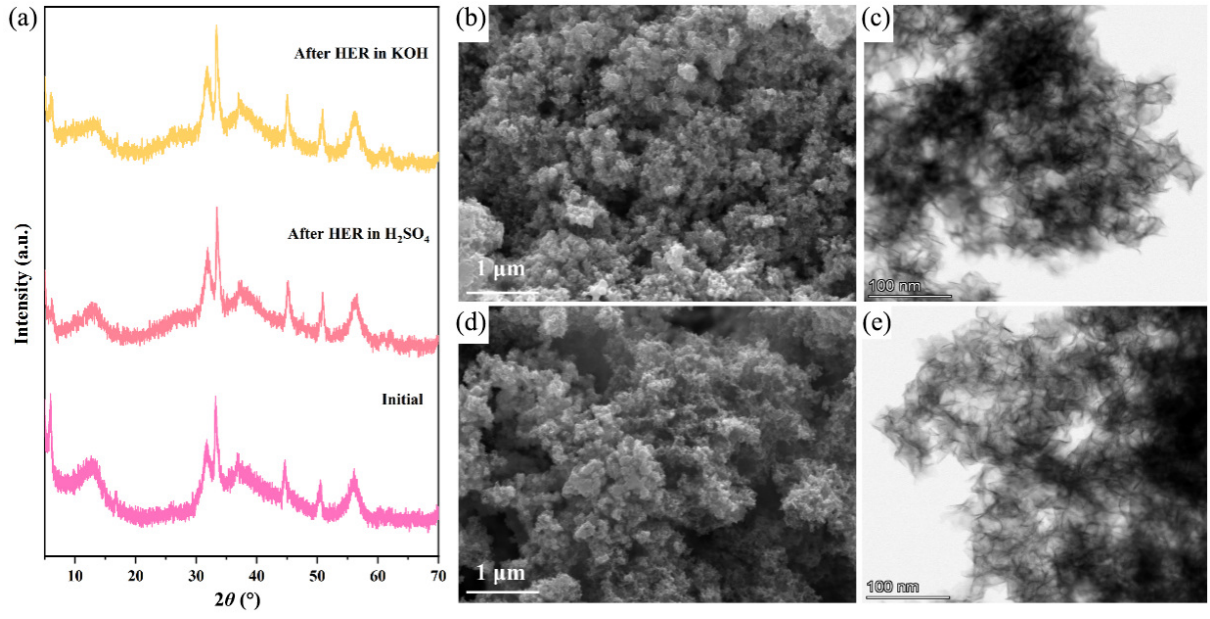

Fig. 11 Composition and morphology characterization of $MoSe_2/Ni_3Se_4/M_4C_3T_x$ after a 24-h stability test: (a) XRD pattern after the stability test; (b) SEM image and (c) TEM image in 0.5 M H_2SO_4; (d) SEM image and (e) TEM image in 1 M KOH.

intrinsically related to its precisely engineered structure that enables optimal reaction kinetics through complementary mechanisms. Electrochemical analysis and structural characterization indicate strong synergistic effects among the constituent components. First, the high-entropy $M_4C_3T_x$ MXene goes beyond serving merely as a conductive substrate. The complex interactions among the five transition metals create a unique electronic environment, resulting in an optimized Fermi level and enhanced electronic conductivity, which ensures rapid electron injection to the active sites. Furthermore, $MoSe_2$ and Ni_3Se_4 nanosheets form tight heterointerfaces on the MXene surface, exposing abundant Mo and Ni edge active sites, while the large specific surface area facilitates fast migration of protons and ions in the electrolyte. These synergistic effects not only optimize the adsorption/desorption kinetics of H^* but also accelerate the transfer of electrons and protons, leading to high activity and long-term stability for the HER. In contrast, $MoSe_2/M_4C_3T_x$, although possessing MXene active sites, lacks the interface modulation and defect engineering provided by Ni_3Se_4, resulting in insufficient interfacial synergy; $MoSe_2/Ni_3Se_4$ lacks the conductive MXene scaffold, limiting electron transport; $Ni_3Se_4/M_4C_3T_x$ is deficient in the active edge sites supplied by $MoSe_2$, leading to sparse catalytic sites; and single-component $MoSe_2$ or f-MXene, despite their intrinsic active sites, lack multicomponent synergy and optimized interfacial structures, exhibiting the lowest overall catalytic efficiency.

The performance difference between acidic and alkaline media primarily originates from the intrinsic distinctions in the HER pathways. In acidic environments, the high concentration of H_3O^+ ions serves as an abundant proton source, enabling the Volmer step to proceed rapidly, with the Heyrovsky step becoming the rate-determining step—a process whose kinetics are effectively optimized by the heterojunction interfaces. In contrast, in alkaline media, the sluggish water dissociation step poses the main challenge. Here, the Ni_3Se_4 component plays a crucial role by providing excellent water-splitting catalytic activity, which, in cooperation with $MoSe_2$, effectively reduces the reaction energy barrier. The variation in ECSA may be related to changes in the electric double-layer structure and surface wettability of the electrode/electrolyte interface under different pH conditions. Overall, the ternary heterostructure achieves efficient adaptability across a wide pH range for the HER through the synergistic and complementary effects of its components.

4 Conclusions

In summary, this study successfully constructed a $MoSe_2/Ni_3Se_4$ heterostructure on a high-entropy $M_4C_3T_x$ MXene substrate via a hydrothermal method. A series of comparative experiments confirmed that this ternary composite exhibits significantly enhanced HER performance compared to the single-component and binary composites, showing excellent catalytic activity and stability in both 0.5 M H_2SO_4 and 1.0 M KOH electrolytes. The performance improvement can be attributed to the following synergistic effects: first, the unique high-entropy MXene substrate not only serves as an excellent conductive bridge to accelerate charge transfer but also effectively modulates the interfacial electronic structure through multielement synergy; second, the tightly coupled heterointerface formed by $MoSe_2$ and Ni_3Se_4 nanosheets on the substrate exposes abundant highly active Mo and Ni edge sites, collectively optimizing the adsorption/desorption kinetics of hydrogen intermediates. This work not only demonstrates the great potential of the "high-entropy MXene substrate/multicomponent active species" design strategy for fabricating efficient and stable HER catalysts but also provides a new design concept and material platform for developing nonnoble metal electrocatalysts suitable for diverse acidic and alkaline environments.

Acknowledgements

This work was supported by the Natural Science Foundation of Hubei Province (No. 2025AFD061) and the National Natural Science Foundation of China (Nos. 52372067, 52402074, 92163208, and 52494933). We acknowledge Dr. Tingting Luo (Center for Materials Research and Analysis Testing, Wuhan University of Technology) for help in S/TEM analysis.

Availability of data and materials

The data that support the findings of this study are available from the corresponding author upon reasonable request.

Competing interests

The authors have no competing interests to declare that are relevant to the content of this article.

Electronic Supplementary Material

Supplementary material is available in the online version of this article at https://doi.org/10.26599/JAC.2025.9221235.

References

[1] Wang ZJ, Meng YZ, Tang SL, *et al.* Simultaneous achievement of large electrocaloric effect and ultra-wide operating temperature range in $BaTiO_3$-based lead-free ceramic. *J Adv Ceram* 2024, **13**: 1234–1241.

[2] Li DX, Zeng XJ, Li ZP, *et al.* Progress and perspectives in dielectric energy storage ceramics. *J Adv Ceram* 2021, **10**: 675–703.

[3] Davis SJ, Lewis NS, Shaner M, *et al.* Net-zero emissions energy systems. *Science* 2018, **360**: eaas9793.

[4] Devlin A, Kossen J, Goldie-Jones H, *et al.* Global green hydrogen-based steel opportunities surrounding high quality renewable energy and iron ore deposits. *Nat Commun* 2023, **14**: 2578.

[5] Pu ZH, Amiinu IS, Cheng RL, *et al.* Single-atom catalysts for electrochemical hydrogen evolution reaction: Recent advances and future perspectives. *Nano-Micro Lett* 2020, **12**: 21.

[6] Li Y, Feng A, Dai LX, *et al.* Progress on the design of electrocatalysts for large-current hydrogen production by tuning thermodynamic and kinetic factors. *Adv Funct Mater* 2024, **34**: 2316296.

[7] Xie LB, Wang LL, Liu X, *et al.* Flexible tungsten disulfide superstructure engineering for efficient alkaline hydrogen evolution in anion exchange membrane water electrolysers. *Nat Commun* 2024, **15**: 5702.

[8] Wang FH, Dong BB, Wang JW, *et al.* Self-supported porous heterostructure WC/WO_{3-x} ceramic electrode for hydrogen evolution reaction in acidic and alkaline media. *J Adv Ceram* 2022, **11**: 1208–1221.

[9] Zhang L, Hu ZH, Huang JT, *et al.* Experimental and DFT studies of flower-like Ni-doped Mo_2C on carbon fiber paper: A highly efficient and robust HER electrocatalyst modulated by $Ni(NO_3)_2$ concentration. *J Adv Ceram* 2022, **11**: 1294–1306.

[10] Zeng XJ, Ye YF, Wang YQ, *et al.* Honeycomb-like MXene/$NiFeP_x$–NC with "continuous"single-crystal enabling high activity and robust durability in electrocatalytic oxygen evolution reactions. *J Adv Ceram* 2023, **12**: 553–564.

[11] Liu YG, Liu S, Li HX, *et al. In-situ* phase conversion of composited 1T@2H–$MoSe_2$ nanosheets with enhanced HER performance. *Mater Chem Phys* 2022, **278**: 125657.

[12] Zhang T, Ye QT, Han ZY, *et al.* Biaxial strain induced OH engineer for accelerating alkaline hydrogen evolution. *Nat Commun* 2024, **15**: 6508.

[13] Liu MQ, Wang JA, Klysubun W, *et al.* Interfacial electronic structure engineering on molybdenum sulfide for robust dual-pH hydrogen evolution. *Nat Commun* 2021, **12**: 5260.

[14] Shi JJ, Bao Y, Ye RR, *et al.* Recent progress and perspective of electrocatalysts for the hydrogen evolution reaction. *Catal Sci Technol* 2025, **15**: 2104–2131.

[15] Inta HR, Ghosh S, Mondal A, *et al.* $Ni_{0.85}Se/MoSe_2$ interfacial structure: An efficient electrocatalyst for alkaline hydrogen evolution reaction. *ACS Appl Energy Mater* 2021, **4**: 2828–2837.

[16] Rameshbabu R, Vinoth V, Pecchi G, *et al.* Novel $MoSe_2$–$Ni(OH)_2$ nanocomposite as an electrocatalyst for high efficient hydrogen evolution reaction. *Int J Hydrog Energy* 2021, **46**: 32471–32479.

[17] Majumdar A, Dutta P, Sikdar A, *et al.* Impact of atomic rearrangement and single atom stabilization on $MoSe_2$@$NiCo_2Se_4$ heterostructure catalyst for efficient overall water splitting. *Small* 2023, **19**: 2207410.

[18] Zhou HQ, Yu F, Huang YF, *et al.* Efficient hydrogen evolution by ternary molybdenum sulfoselenide particles on self-standing porous nickel diselenide foam. *Nat Commun* 2016, **7**: 12765.

[19] Wu PY, Sun GY, Chen YZ, *et al.* $MoSe_2$–Ni_3Se_4 hybrid nanoelectrocatalysts and their enhanced electrocatalytic activity for hydrogen evolution reaction. *Nanoscale Res Lett* 2020, **15**: 132.

[20] Guo KL, Wang YT, Huang JF, *et al.* Symbiotic Ni_3Se_4/Ni heterostructure induced by unstable $NiSe_2$ for enhanced hydrogen generation. *Chem Eng J* 2023, **454**: 140488.

[21] Zhang ZL, Liang T, Jin CL, *et al.* Synergistically coupling CoS/FeS_2 heterojunction nanosheets on a MXene via a dual molten salt etching strategy for efficient oxygen evolution reaction. *J Mater Chem A* 2024, **12**: 14517–14530.

[22] Lim KRG, Shekhirev M, Wyatt BC, *et al.* Fundamentals of MXene synthesis. *Nat Synth* 2022, **1**: 601–614.

[23] Zhou TZ, Wu C, Wang YL, *et al.* Super-tough MXene-functionalized graphene sheets. *Nat Commun* 2020, **11**: 2077.

[24] Wan SJ, Chen Y, Huang CJ, *et al.* Scalable ultrastrong MXene films with superior osteogenesis. *Nature* 2024, **634**: 1103–1110.

[25] Nemani SK, Zhang BW, Wyatt BC, *et al.* High-entropy 2D carbide MXenes: $TiVNbMoC_3$ and $TiVCrMoC_3$. *ACS Nano* 2021, **15**: 12815–12825.

[26] Du ZG, Wu C, Chen YC, *et al.* High-entropy atomic layers of transition-metal carbides (MXenes). *Adv Mater* 2021, **33**: 2101473.

[27] Qiao LJ, Bi JQ, Liang GD, *et al.* Synthesis of high-entropy MXenes with high-efficiency electromagnetic wave absorption. *J Adv Ceram* 2023, **12**: 1902–1918.

[28] Yan YN, Huang XP, Yan XH, *et al.* New ultra-high cycle stable accordion-like high entropy MXene with improving energy storage performance of supercapacitors. *Adv Funct Mater* 2025, **35**: 2420578.

[29] Liang Q, Wang SZ, Lu XM, *et al.* High-entropy MXene as bifunctional mediator toward advanced Li–S full batteries. *ACS Nano* 2024, **18**: 2395–2408.

[30] Zou HR, Zhang W, Zhang JY, *et al.* Synthesis of a novel textured high entropy M_4AlC_3 (M = Ti, V, Mo, Nb, Ta) composites with improved mechanical properties *via* spark plasma sintering. *J Eur Ceram Soc* 2024, **44**: 6889–6900.

[31] Alhabeb M, Maleski K, Anasori B, *et al.* Guidelines for synthesis and processing of two-dimensional titanium carbide ($Ti_3C_2T_x$ MXene). *Chem Mater* 2017, **29**: 7633–7644.

[32] Downes M, Shuck CE, McBride B, *et al.* Comprehensive synthesis of $Ti_3C_2T_x$ from MAX phase to MXene. *Nat Protoc* 2024, **19**: 1807–1834.

[33] Qiao LJ, Bi JQ, Liang GD, *et al.* Synthesis and electromagnetic wave absorption performances of a novel $(Mo_{0.25}Cr_{0.25}Ti_{0.25}V_{0.25})_3AlC_2$ high-entropy MAX phase. *J Mater Sci Technol* 2023, **137**: 112–122.

[34] Naguib M, Kurtoglu M, Presser V, *et al.* Two-dimensional nanocrystals: Two-dimensional nanocrystals produced by exfoliation of Ti_3AlC_2. *Adv Mater* 2011, **23**: 4207.

[35] Dai TJ, Sun J, Peng XS, *et al. In situ* synthesis of heterogeneous $NiSe_2$ /$MoSe_2$ nanocomposite for high-efficiency electrocatalytic hydrogen evolution reaction. *Energy Sci Eng* 2022, **10**: 4061–4070.

[36] Zhu M, Yan Q, Xue YQ, *et al.* Free-standing P-doped $NiSe_2/MoSe_2$ catalyst for efficient hydrogen evolution in acidic and alkaline media. *ACS Sustainable Chem Eng* 2022, **10**: 279–287.

[37] Zong H, Yu K, Zhu ZQ. Heterostructure nanohybrids of Ni-doped $MoSe_2$ coupled with Ti_2NT_x toward efficient overall water splitting. *Electrochim Acta* 2020, **353**: 136598.

[38] Wang HS, Meng LX, Liu SY, *et al.* Ni-based multi-interface engineering on MXene ($Ti_3C_2T_x$) modified electrode for all-pH-value hydrogen evolution. *Chem Eng J* 2023, **476**: 146929.

[39] Wang T, Wu HM, Feng CQ, *et al.* MoP@NiCo-LDH on nickel foam as bifunctional electrocatalyst for high efficiency water and urea–water electrolysis. *J Mater Chem A* 2020, **8**: 18106–18116.

[40] Yu QP, Fu YX, Zhao JR, *et al.* Boron doping activate strong metal-support interaction for electrocatalytic hydrogen evolution reaction in full pH range. *Appl Catal B Environ* 2023, **324**: 122297.

[41] Sun YQ, Hang LF, Shen Q, *et al*. Mo doped Ni_2P nanowire arrays: An efficient electrocatalyst for the hydrogen evolution reaction with enhanced activity at all pH values. *Nanoscale* 2017, **9**: 16674–16679.
[42] Yu J, Li WJ, Zhang HS, *et al*. Metallic $FePSe_3$ nanoparticles anchored on N-doped carbon framework for All-pH hydrogen evolution reaction. *Nano Energy* 2019, **57**: 222–229.
[43] Kuang PY, Tong T, Fan K, *et al*. *In situ* fabrication of Ni–Mo bimetal sulfide hybrid as an efficient electrocatalyst for hydrogen evolution over a wide pH range. *ACS Catal* 2017, **7**: 6179–6187.
[44] Yang MJ, Zhang Y, Jian JH, *et al*. Donor–acceptor nanocarbon ensembles to boost metal-free all-pH hydrogen evolution catalysis by combined surface and dual electronic modulation. *Angew Chem Int Ed* 2019, **58**: 16217–16222.
[45] Ma MJ, Xu JH, Wang HQ, *et al*. Multi-interfacial engineering of hierarchical $CoNi_2S_4/WS_2/Co_9S_8$ hybrid frameworks for robust all-pH electrocatalytic hydrogen evolution. *Appl Catal B Environ* 2021, **297**: 120455.
[46] Zhu M, Zhang DF, Lu Q, *et al*. Hollow hexagonal NiSe–Ni_3Se_2 anchored onto reduced graphene oxide as efficient electrocatalysts for hydrogen evolution in wide-pH range. *Int J Hydrog Energy* 2021, **46**: 20524–20533.
[47] Yang Y, Yao HQ, Yu ZH, *et al*. Hierarchical nanoassembly of $MoS_2/Co_9S_8/Ni_3S_2$/Ni as a highly efficient electrocatalyst for overall water splitting in a wide pH range. *J Am Chem Soc* 2019, **141**: 10417–10430.
[48] Wang HQ, Xu JH, Zhang QB, *et al*. Super-hybrid transition metal sulfide nanoarrays of Co_3S_4 nanosheet/P-doped WS_2 nanosheet/Co_9S_8 nanoparticle with Pt-like activities for robust all-pH hydrogen evolution. *Adv Funct Mater* 2022, **32**: 2112362.
[49] Kang YQ, Cretu O, Kikkawa J, *et al*. Mesoporous multimetallic nanospheres with exposed highly entropic alloy sites. *Nat Commun* 2023, **14**: 4182.
[50] Murthy AP, Theerthagiri J, Madhavan J. Insights on tafel constant in the analysis of hydrogen evolution reaction. *J Phys Chem C* 2018, **122**: 23943–23949.